RESEARCH ARTICLE | APRIL 01 2025

Scaling properties of nonstationary wind fields based on time-varying mean wind speed models

Kang Cai (蔡康) ; Mingfeng Huang (黄铭枫) ; Jiayao Wang (王佳瑶) ; You Dong (董优) ; Yi-Qing Ni (倪一清) ; Pak-wai Chan (陈柏纬)

Physics of Fluids 37, 045108 (2025)
https://doi.org/10.1063/5.0256119

Physics of Fluids ARTICLE pubs.aip.org/aip/pof

Scaling properties of nonstationary wind fields based on time-varying mean wind speed models

Cite as: Phys. Fluids **37**, 045108 (2025); doi: 10.1063/5.0256119
Submitted: 2 January 2025 · Accepted: 12 March 2025 ·
Published Online: 1 April 2025 · Corrected: 8 April 2025

Kang Cai (蔡康),[1,2,3,4,a)] Mingfeng Huang (黄铭枫),[1,2,b)] Jiayao Wang (王佳瑶),[3,b)] You Dong (董优),[3,c)] Yi-Qing Ni (倪一清),[3,4,d)] and Pak-wai Chan (陈柏纬)[5,e)]

AFFILIATIONS

[1]Institute of Structural Engineering, College of Civil Engineering and Architecture, Zhejiang University, Hangzhou 310058, People's Republic of China
[2]School of Civil Engineering and Architecture, Guangxi University, Nanning 530004, People's Republic of China
[3]Department of Civil and Environmental Engineering, The Hong Kong Polytechnic University, Hung Hom, Kowloon, Hong Kong Special Administrative Region, People's Republic of China
[4]Hong Kong Branch of the National Engineering Research Center on Rail Transit Electrification and Automation, Hung Hom, Kowloon, Hong Kong Special Administrative Region, People's Republic of China
[5]Hong Kong Observatory, Hong Kong Special Administrative Region, People's Republic of China

[a)]**Electronic mail**: kangc_hk@163.com
[b)]**Authors to whom correspondence should be addressed:** mfhuang@zju.edu.cn and jiayao.wang@connect.ust.hk
[c)]**Electronic mail**: you.dong@polyu.edu.hk
[d)]**Electronic mail**: ceyqni@polyu.edu.hk
[e)]**Electronic mail**: pwchan@hko.gov.hk

ABSTRACT

This paper introduces an approach designed to address an inadequacy of Taylor's frozen hypothesis in determining the scaling exponent of structure functions for nonstationary wind speeds. The key step of this approach is to substitute the time-varying mean (TVM) components $\bar{U}(t)$ for the constant mean $\bar{U}$ in the calculation of structure functions of nonstationary wind speed fields. In this approach, TVM components of nonstationary wind speeds were first determined based on the advanced wavelet transform and empirical mode decomposition. Subsequently, a comprehensive comparison was conducted for the calculation of scaling exponents of nonstationary wind speed records measured during Typhoon and Downburst events, utilizing different approaches. Our analysis results reveal that various models, including the K41 model [A. N. Kolmogorov, "The local structure of turbulence in incompressible viscous fluid for very large Reynolds' numbers," Proc. USSR Acad. Sci. **30**, 301–305 (1941), available at https://scispace.com/papers/the-local-structure-of-turbulence-in-incompressible-viscous-25te3acxv9], K62 model [A. Kolmogorov, "A refinement of previous hypotheses concerning the local structure of turbulence in a viscous incompressible fluid at high Reynolds number," J. Fluid Mech. **13**(1), 82–85 (1962)], β model [Frisch *et al.*, "A simple dynamical model of intermittent fully developed turbulence," J. Fluid Mech. **87**(4), 719–736 (1978)], and SL model [She and Leveque, Universal scaling laws in fully developed turbulence," Phys. Rev. Lett. **72**(3), 336–339 (1994)], have their own respective strengths and limitations in describing the relationship between the scaling exponent ξ_p and the order p. Significant differences in scaling exponents were observed between the original and new versions of Taylor's hypothesis, particularly at higher orders of p or for wind speed with strong nonstationarity such as the downburst. It is suggested that the Taylor's frozen hypothesis needs to be adjusted when computing the scaling exponents ξ_p of nonstationary wind speed fields in future studies.

I. INTRODUCTION

Turbulence is a common phenomenon where the velocity fluctuates significantly with a hierarchical process in which energy transfers from large to small scales (Frisch and Kolmogorov, 1995). A way to investigate the statistical behavior of turbulence is often achieved via the p th-order structure function that provides basic knowledge for the analysis of the scaling properties of fully developed turbulence (Harris *et al.*, 1977). A key piece of information on the small-scale motion in

turbulence lies in the p th-order structure function that is defined as the successive moment of longitudinal velocity difference $\delta u_r = u(x+r) - u(x)$ over a spatial separation distance, r, of two points $x + r$ and x, given by

$$S_p(r) = \langle |\delta u_r|^p \rangle, \tag{1}$$

where the angular bracket $\langle \cdots \rangle$ stands for the ensemble average, p denotes the order of moment and r is parallel to u. Different from the longitudinal situation, the lateral structure function was calculated as follows:

$$S_p^w(r) = \langle |\delta w_r|^p \rangle, \tag{2}$$

where w denotes the lateral wind speeds ($\delta w_r = w(x+r) - w(x)$). In this case, r is perpendicular to w.

Typically, there are two characteristic scales of interest in turbulence analysis: the dissipation scale $\eta = \left(\frac{\nu^3}{\langle \varepsilon \rangle}\right)^{\frac{1}{4}}$ and the integral scale $L = \int \rho_\tau d\tau$, where ν, $\langle \varepsilon \rangle$, and ρ_τ are, respectively, the kinematic viscosity, mean energy dissipation rate, and autocorrelation coefficient (Ali *et al.*, 2016). The parameter η characterizes the smallest scales of fluctuations. The integral scale L can be regarded as the size of the largest eddies in the turbulent flow (Ruiz-Chavarria *et al.*, 2000). When the separation distance r is smaller than η, the velocity field is regular. When $\eta < r < L$, this range is referred to as the inertial range and is of significant interest in the study of turbulent flow.

For homogenous and isotropic turbulent flows, Kolmogorov (1941) (hereafter K41) introduced a universal theory stating that the mean energy dissipation rate, $\langle \varepsilon \rangle$, is scale invariant. As a result, the corresponding structure function $S_p(r)$ was formulated as

$$S_p(r) \sim \langle \varepsilon \rangle^{\frac{p}{3}} r^{\frac{p}{3}}. \tag{3}$$

However, experimental results of high-order statistics, shown in Meneveau and Sreenivasan (1991), reveal notable discrepancies with K41 when considering intermittency. This finding suggests that the scaling exponent exhibits nonlinear behavior with respect to p, rather than remaining linear. In response to this discrepancy, Kolmogorov (1962) (K62) modified the K41 theory by assuming a lognormal distribution for scale dependence within the dissipation range, and got

$$S_p(r) \sim r^{\xi_p}. \tag{4}$$

Here, ξ_p is the scaling exponent. The possible existence of a universal scaling exponent ξ_p has been one of the most exciting aspects of turbulence research. Over time, several widely accepted expressions have been proposed to present the relationship between ξ_p and the order p. One such expression is the above K62 model, described as

$$\xi_p = \frac{p}{3} + \frac{1}{18}\mu p(3-p), \tag{5}$$

where μ denotes the intermittency exponent quantifying the intermittency of energy dissipation in turbulent flows. This parameter can be determined as $\mu = 2 - \xi_6$, as reported by Böttcher *et al.* (2007). The lognormal model predicts a maximum of the exponent ξ_p at $p = \frac{1}{2}(6/\mu + 3)$. The currently accepted value of μ is $\mu \approx 0.2$, in which case the maximum of p would reach 16 (Water and Herweijer, 1999). Thus, the maximum order of structure functions in this paper is set as 16. A detailed description of the K62 model can be found in Galtier (2016). Additionally, Frisch *et al.* (1978) introduced the β model, also known as the fractal model. This model is based on the concept of a fractal cascade, and focuses on the transmission of nonlinearity in the inertial subrange to calculate the scaling exponent, as follows:

$$\xi_p = \frac{p}{3} + \frac{1}{3}\mu(3-p). \tag{6}$$

She and Leveque (1994) developed a model (abbreviated as the SL model) to estimate the scaling exponent by considering its dependence on the hierarchical structure of energy dissipation, given by

$$\xi_p = \frac{p}{9} + 2\left(1 - \left(\frac{2}{3}\right)^{p/3}\right). \tag{7}$$

These models contribute to our understanding of turbulent scaling behavior and provide valuable tools for turbulence research.

The scaling properties of wind turbulence have been investigated for different types of flows such as atmospheric boundary layer flow (Vindel *et al.*, 2008), wake flow around a cylinder (Gaudin *et al.*, 1998), and direct numerical simulation homogenous flow (Vincent and Meneguzzi, 1991). The computation of structure function $S_p(r)$ in most of these studies can be classified into two categories. One is the direct measurement of spatial velocity increments using the particle image velocimetry (PIV) method (Saw *et al.*, 2016, 2018), where the velocity field can be built across the quasi-two-dimensional laser sheet by employing peak correlation over small interrogation windows. Another involves the one-point velocity measurements based on a propeller anemometer or ultrasonic anemometer. It can be used to compute the structure function only via Taylor's frozen flow hypothesis, $r = \bar{U} \cdot \Delta t$ (Taylor, 1938), where $\bar{U}$ is the mean velocity at the specified location. In such a situation, $S_p(r) \sim r^{\xi_p}$ can be accurately converted to

$$S_p(\Delta t) = \left\langle |u(t+\Delta t) - u(t)|^p \right\rangle \sim \Delta t^{\xi_p}, \tag{8}$$

if the velocity of the turbulent flow is stationary (i.e., its mean is constant rather than time-variant). Accordingly, an accurate determination of the scaling exponent of wind can be achieved solely through single-point measurement $u(t)$. Most of the experimental reports employing the second method were from turbulent flows with an open geometry (e.g., turbulence downstream of grids, jets, and the atmospheric boundary layer) where there exists a strong flow. A summary of these results can be found in the work of Arneodo *et al.* (1996). It is worth noting that the common practice is to keep the turbulence intensity $I = \sigma/\bar{U}$ small, preferably below 10% (σ denoting the standard deviation of the velocity) (Saw *et al.*, 2018). Whereas, recent research has shown that wind speed fields in extreme wind conditions, such as tropical cyclones, thunderstorms, downbursts, and strong winds, exhibit significant nonstationary characteristics (Gurley and Kareem, 1997; Wood *et al.*, 2001; Jung and Masters, 2013; and Solari *et al.*, 2015). As a result, the overall wind speed series in these cases needs to be considered as the combination of the fluctuating component and the time-varying mean (TVM) component rather than a constant mean $\bar{U}$. Furthermore, Cai *et al.* (2022) reported that the turbulence intensity of nonstationary wind speeds measured during

Typhoon Mangkhut landing was far more than 10%, regardless of the adoption of a stationary wind model (i.e., constant mean) or a nonstationary wind model (i.e., TVM). Consequently, this raises questions regarding the applicability of Taylor's frozen hypothesis in the context of nonstationary wind fields.

To address this issue, the primary objective of this study is to adjust Taylor's frozen hypothesis and then study the scaling properties of nonstationary winds such as typhoon and downburst events. The paper is organized as follows: Sec. II A presents two advanced extraction methods for the TVM of nonstationary wind speeds. In Sec. II B, a new version of Taylor's frozen hypothesis is proposed based on the nonstationary wind model. Section II C introduces a commonly adopted extended self-similarity method (ESS) (Benzi *et al.*, 1993) for studying the scaling properties of wind speeds. A comprehensive comparison is conducted on scaling exponents using different approaches for nonstationary typhoon and downburst wind speeds in Secs. III and IV, respectively. Finally, some concluding remarks are given in Sec. V.

II. METHODOLOGY

A. Extraction of the time-varying mean

The TVM of the nonstationary wind speed may be extracted by the advanced wavelet transform (WT) method developed by Cai *et al.* (2022). Accordingly, the measured wind speed $u(t)$ is decomposed as

$$u(t) = \sum_{j=1}^{M} D_j(t) + A_M(t), \tag{9}$$

where M is the total number of decomposition levels, $D_j(t)$ denotes the detail function of the wavelet transform at decomposition level j, and $A_M(t)$ is the approximation function. Some TVMs of $u(t)$ could be presented as the sum of the approximation component $A_M(t)$ and S (non-negative integer) detail parts $D_j(t)$,

$$\bar{U}(t)_S = \begin{cases} A_M(t), & S = 0, \\ \sum_{j=M+1-s}^{M} D_j(t) + A_M(t), & 1 \le S \le M-1. \end{cases} \tag{10}$$

Notably, Cai *et al.* (2021a, 2021b) presented the definition of an optimal TVM from the structural wind engineering perspective (i.e., optimal TVM is the one that can reflect the time-varying trend of the wind speed data, but not cause an obvious dynamic response of structures), and developed, accordingly, two restrictive conditions to identify and extract the optimal TVM. It is suggested that the optimal TVM of a 10-min time history of wind speeds should meet both of the following conditions: (1) the probability density function of fluctuating wind component needs to agree with the modified Gaussian function rather than the traditional Gaussian distribution (Condition I); and (2) the number of local maxima of the obtained optimal TVM within a 10-min time interval is less than six (Condition II). Condition I imposes relatively lenient constraints on the probability density function of fluctuating components when compared to the assumptions of Gaussian distribution. Cai *et al.* (2022) have shown that Condition I is consistently satisfied when the associated TVM is derived using the aforementioned WT method, leaving only Condition II to be fulfilled. Condition II is established from a wind engineering perspective, considering the TVM as a static load on structures. Assuming that the upper-frequency limit w_f of the TVM derived from nonstationary wind speed record is below 0.01 Hz, the dynamic magnification factor, D, approaches unity, as $D = \left[\left(1-\beta^2\right)^2 + (2\varepsilon\beta)^2\right]^{-1/2} \le 1.0101$ as indicated by Cai *et al.* (2021a, 2021b). Here, ε represents the damping ratio of the structure, and β is the ratio of the applied loading frequency $w_f\,(Hz)$ to the natural frequency $w\,(Hz)$ of the structure. Given the frequency limit of $w_f = \frac{1}{T} \le 0.01Hz$, it can be deduced that the period of the calculated TVM T is at least 100 seconds. Consequently, the associated TVM can be expected to encompass approximately six cycles for a fixed time duration of 10 min. Therefore, the number of local maxima in the calculated TVM should not exceed six. With this restriction, the optimal TVM is the one in Eq. (10), which has the largest number of local maxima, but no more than 6 with a time interval of 10 min. Subsequently, the relative fluctuating component $u'(t)$ is given by

$$u'(t) = \sum_{i=1}^{M-s} D_i(t). \tag{11}$$

Considering that the type of initial mother wavelet has an insignificant effect on the candidate TVMs, and that the Debauchies wavelet with a higher vanishing moment could provide a better reconstruction quality (Cai *et al.*, 2022), the classical Daubechies wavelet of order 12 has been selected as the initial mother wavelet for this study, with the total number of decomposition levels $M = 12$, in accordance with the recommendations of Cai *et al.* (2022).

For further comparison, the empirical mode decomposition (EMD) will be also employed to extract the TVM. Accordingly, original time histories may be expressed as the sum of several intrinsic mode functions $C_j(t)$ and the final residue $R_N(t)$,

$$u(t) = \sum_{j=1}^{N} C_j(t) + R_N(t). \tag{12}$$

The superposition of the residue $R_N(t)$ and the last $C_j(t)$ can be regarded as the TVM from the recorded wind speed time history. The detailed process can be found in Xu and Chen (2004) and Chen *et al.* (2007).

B. Taylor's frozen hypothesis

Based on the previous discussion, it becomes apparent that Taylor's frozen hypothesis is inapplicable for determining scaling properties of nonstationary wind fields. As a result, it is necessary to refine this hypothesis to obtain a more convincing estimate.

According to traditional Taylor's frozen hypothesis, it assumes that the mean wind speed $\bar{U}$ remains constant and the spatial distance is determined by the relationship $r = \bar{U} \cdot \Delta t$. Using this relationship, the structure function $S_p(r)$ at a given spatial distance r can be readily calculated by Eq. (13), which is based on the one-point velocity measurements $u(t)$ represented by the blue dots in Fig. 1,

$$\begin{aligned} S_p(r) &= \frac{1}{k}\sum_{i=1}^{k}\left(\left|u(x_i+r) - u(x_i)\right|^p\right) \\ &= \frac{1}{k}\sum_{i=1}^{k}\left(\left|u(t_i+\Delta t_i) - u(t_i)\right|^p\right). \end{aligned} \tag{13}$$

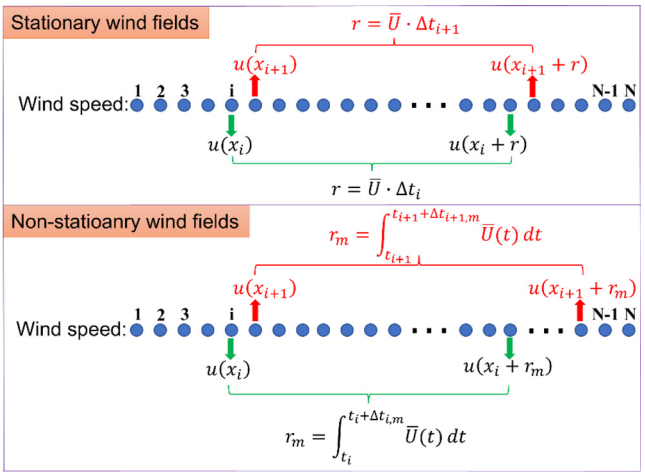

FIG. 1. Taylor's frozen hypotheses for stationary and nonstationary wind fields.

It is evident that the time gap Δt is constant at different instant times t_i for the same spatial distance r, meaning that $\Delta t_i = \Delta t_{i+1}$ as illustrated in the upper part of Fig. 1.

The key step of the new approach is to substitute the TVM $\bar{U}(t)$ for the constant mean $\bar{U}$ in Taylor's frozen hypothesis. The spatial distance r_m is then modified as

$$r_m = \int_{t_i}^{t_i+\Delta t_{i,m}} \bar{U}(t)dt. \tag{14}$$

Considering that $\bar{U}(t)$ is always greater than zero, it follows that the integral $\int_{t_i}^{t_i+\Delta t_{i,m}} \bar{U}(t)dt$ increases as $\Delta t_{i,m}$ increases. This implies that a unique $\Delta t_{i,m}$ can be found such that $\mathrm{r_m} - \int_{\mathrm{t_i}}^{\mathrm{t_i}+\Delta \mathrm{t_{i,m}}} \bar{\mathrm{U}}(\mathrm{t})\mathrm{dt} = 0$ at each instant time t_i for the given r_m. Once the distance sequence $\{r_m\,(m = 1, 2, \ldots, n)\}$ to be analyzed is determined, the time interval $\Delta t_{i,m}$ for every r_m can be obtained by utilizing Eq. (14) at each instant time t_i. Then, the expression $S_p(r) \sim r^{\xi_p}$ in Eq. (4) could be replaced by

$$S_p(r_m) \sim r_m{}^{\xi_p}, \tag{15}$$

where $S_p(r_m) = \left\langle \left| u(x + r_m) - u(x) \right|^p \right\rangle = \left\langle \left| u(t_i + \Delta t_{i,m}) - u(t_i) \right|^p \right\rangle$. Subsequently, the scaling exponent ξ_p could be obtained by the linear fitting between the values of $\log_2(r_m)$ and $\log_2(S_p(r_m))$. It should be noted that the time gap $\Delta t_{i,m}$ is not fixed for a given r_m, but varies with the position x or time t, as $\bar{U}(t)$ is time-variant. That is to say that the time gap $\Delta t_{i,m}$ at time t_i is not necessarily equal to $\Delta t_{i+1,m}$ at time t_{i+1} for the same distance r_m, as shown in the bottom part of Fig. 1. The detailed process for estimating the scaling exponent of the structure function is summarized in Fig. 2. Furthermore, it is worth noting that if $\bar{U}(t)$ in Eq. (14) takes the constant mean of wind speeds, the new method discussed in this section becomes equivalent to the original Taylor's frozen hypothesis, meaning that this approach can be applied to calculate scaling exponents of stationary wind speeds as well. As a result, the Taylor's frozen hypothesis can be regarded as a special case of the new technique.

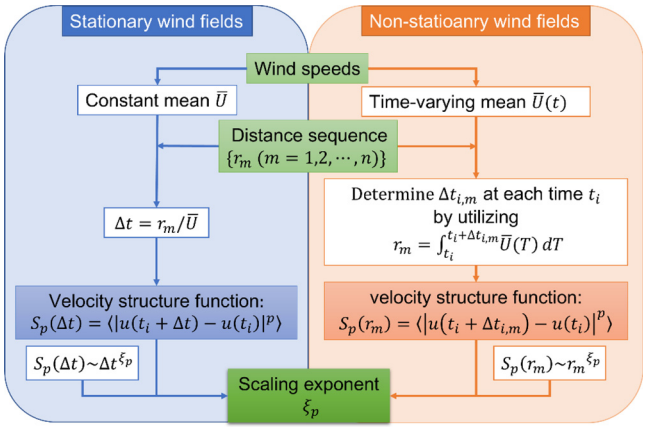

FIG. 2. The scaling exponent ξ_p for stationary and nonstationary wind fields.

C. Extended self-similarity method

It is worth noting that a low Reynolds number is associated with a short inertial subrange, making the scaling behavior either difficult to distinguish or nonexistent (Ali *et al.*, 2016). To overcome this obstacle, Benzi *et al.* (1993) found that the scaling properties could be expanded up to the dissipative range and developed the extended self-similarity (ESS) method to yield the scaling exponent. The idea of this technique is to represent the quantity $S_p(r)$ as a function of the third-order structure function $S_3(r)$ rather than the spatial separation distance r, as follows:

$$S_p(r) \sim (S_3(r))^{\xi_p}. \tag{16}$$

The scaling exponents ξ_p are the slope of the fitted line after plotting $\log_2(S_p(r))$ against $\log_2(S_3(r))$. The significant point about the ESS method is that this relation is applied to not only fully developed turbulence but also low-to-moderate turbulence where $S_p(r) \sim r^{\xi_p}$ is not applicable (Briscolini *et al.*, 1994). Furthermore, the relation expressed in Eq. (16) presents a much wider range of scales than Eq. (4). Notably, the ESS method has been successfully applied to low- and high- Reynolds number flows found in Babiano *et al.* (1997), as well as the homogeneous and non-homogeneous flows reported by Arneodo *et al.* (1996) and Gaudin *et al.* (1998). It is therefore more suitable and reliable to employ the ESS method to investigate the scaling properties of nonstationary wind fields in this study.

III. SCALING PROPERTIES OF NONSTATIONARY TYPHOON WIND FIELDS

A. Data source

During the landfall of Super Typhoon Mangkhut, from September 15 to September 18, 2018, wind speed data were continuously recorded using four three-dimensional (3 D) sonic anemometers. These instruments, each boasting an accuracy of ±0.1 m/s and a sampling frequency of 10 Hz, were strategically positioned at heights of 10, 40, 160, and 320 m above ground level on a 356 m tall meteorological gradient tower in Shenzhen, China (22°38′59″N, 113°53′36″E). A more comprehensive description of the instrumentation utilized in this study is available in Cai *et al.* (2022).

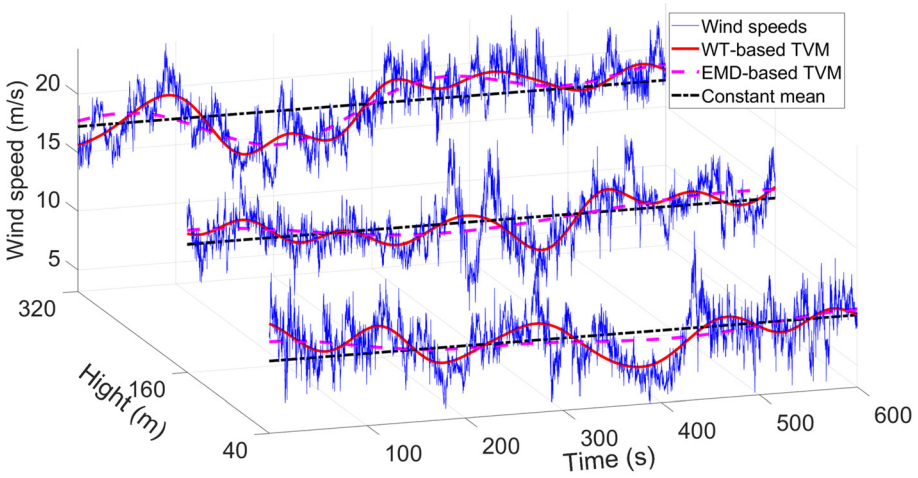

(a) Longitudinal wind speed samples and associated TVMs

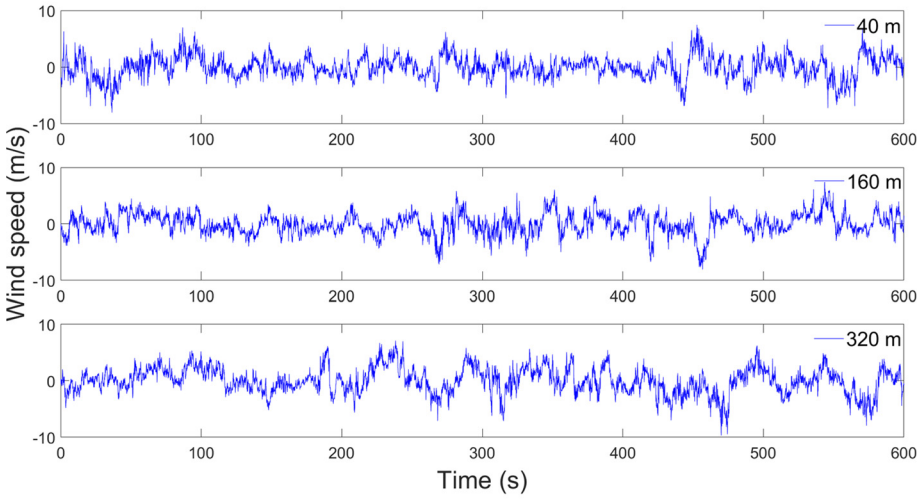

(b) Lateral wind speed samples

FIG. 3. 10-min wind speed samples measured at different heights during Typhoon Mangkhut.

B. The comparison of scaling exponents

In this paper, the 10-minute sample of wind speed, which includes both longitudinal and lateral components synchronously measured at three high heights of 40, 160, and 320 meters serves as a case study to illustrate the analytical process. Two types of TVMs were obtained under a nonstationary framework as described in Sec. II A, utilizing both WT-based and EMD-based methods, as shown in Fig. 3. For comparative purposes, a model with a constant mean was also evaluated. The results demonstrate that the TVM derived from the WT-based method captures more detailed local fluctuations in wind speed than both the EMD-based TVM and the constant mean model.

Notably, the average of Eqs. (1) and (2) can be trivially written as an integral over the probability density function $F(\delta\alpha_r)(\alpha = u, w)$ of velocity increments $\delta\alpha_r$. Thus, the structure function $S_p(r)$ is the p th moment of the probability density function $F(\delta\alpha_r)$ (Water and Herweijer, 1999). After the time gap $\Delta t_{i,m}$ at every instantaneous time t_i was obtained utilizing Eq. (14) for the specified r_m based on different means including the WT-based TVM, EMD-based TVM, and constant mean, the natural logarithms of the probability density functions $F(\delta\alpha_r)$ for the longitudinal and lateral velocity increments $\delta\alpha_r$ were then obtained at the three representative spatial distances of L1 = 20 m, L2 = 50 m, and L3 = 150 m for the wind speed sample at the height of 320 m, as shown in Fig. 4. While the probability distribution maps for the same spatial distances based on different approaches were similar in the middle part, there exist some differences at both ends. In addition, Fig. 4 also reveals that the larger the separation distances are, the higher the wings on both sides are.

Based on the velocity increments $\delta\alpha_r(\alpha = u, w)$ for the wind speed sample at the height of 320 m, higher order statistic skewness, $Sk = \frac{\langle(\delta\alpha_r)^3\rangle}{\langle(\delta\alpha_r)^2\rangle^{3/2}}$, and Kurtosis, $Ku = \frac{\langle(\delta\alpha_r)^4\rangle}{\langle(\delta\alpha_r)^2\rangle^2}$, are determined for each spatial distance, as depicted in Fig. 5. For the longitudinal wind speed,

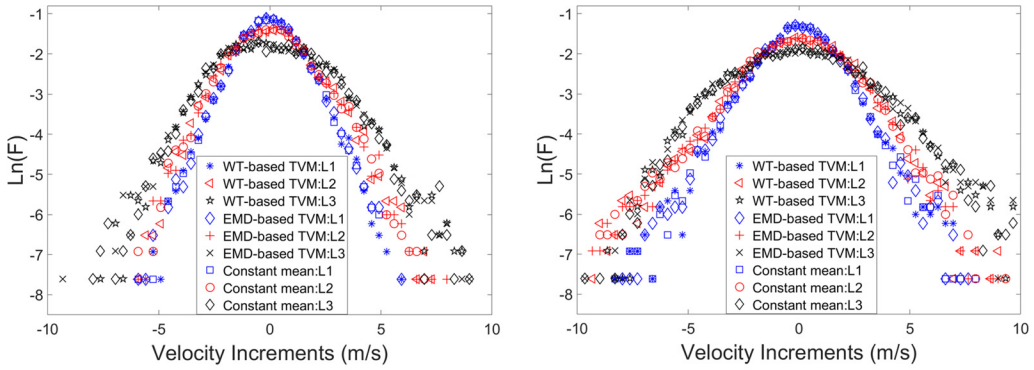

FIG. 4. The natural logarithm of the probability density function F of the velocity increments for the wind speed sample at the height of 320 m based on different methods at the spatial distance of L1 = 20 m, L2 = 50 m, and L3 = 150 m.

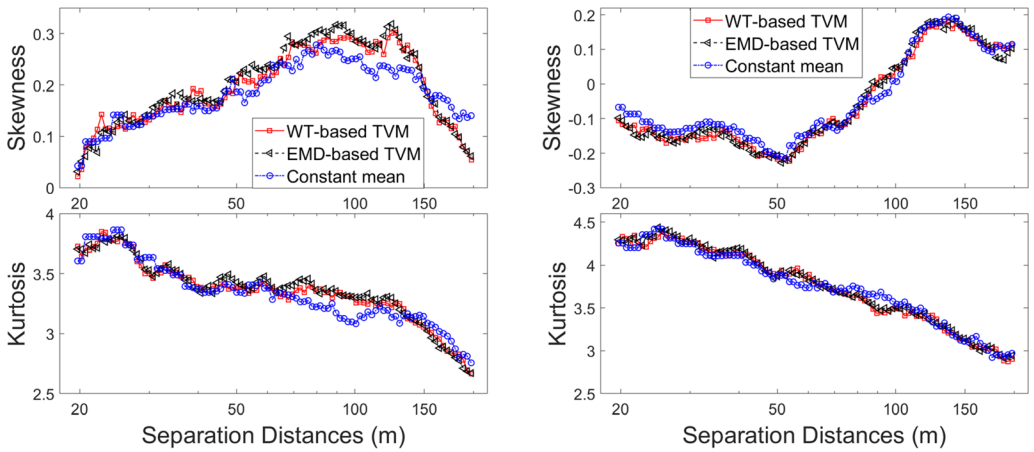

FIG. 5. The skewness and kurtosis of velocity increments for the wind speed sample at the height of 320 m with the increase in separation distances utilizing different approaches.

it is evident that the skewness increases gradually with increasing spatial separation distance and then sharply decreases, and the values are all greater than zero. It indicates that their probability distributions are right-skewed. Water and Herweijer (1999) gave a reason for this phenomenon—in the longitudinal configuration, the possibility of conveying information from the point x to the point $x + r$ depends on the sign of the velocity increments δu_r, leading to the asymmetry of the probability density function $F(\delta u_r)$. In terms of the lateral wind component, the associated skewness is not always larger than zero. That is because in these two cases with the velocity $w(x)$ and $w(x + r)$ perpendicular to r, no such asymmetry can exist for homogeneous turbulence (Water and Herweijer, 1999). Meanwhile, kurtosis is a measure that describes how heavily the tails of a distribution differ from the tails of a normal distribution. It is obvious that there is a gradual reduction in kurtosis even less than 3 in Fig. 5 for these cases, which indicates that the tail of the distribution becomes lighter with the increase in separation distances. Meanwhile, it verifies the observation from Fig. 4 that with increasing separation distances, the higher the wings of the probability distribution maps in both sides are. Additionally, it should be noted that the disparities in both kurtosis and skewness are less pronounced when using WT-based TVM and EMD-based TVM.

The analysis results using the ESS method at different orders $p = 2$, 9, and 16 were computed and provided in Fig. 6 for the longitudinal wind speeds. The strong linear relation between $\log_2(S_p(r))$ and $\log_2(S_3(r))$ in Fig. 6 demonstrates the validity of the ESS method for calculating the scaling exponent ξ_p of wind speeds for the low order $p = 2$. With the increase in p, although the associated linear relationship of $\log_2(S_p(r))$ and $\log_2(S_3(r))$ gradually weakens from Fig. 6, a reliable scaling exponent can be still yielded. Hence, the values of ξ_p for the longitudinal and lateral wind speed components were calculated using this reliable ESS method when taking the order $p = 2$–16, as described in Figs. 7 and 8. Meanwhile, the wind speed series measured synchronously at other two heights (40 and 160 m) were subjected to the same operation. For comparison, Figs. 7 and 8 also

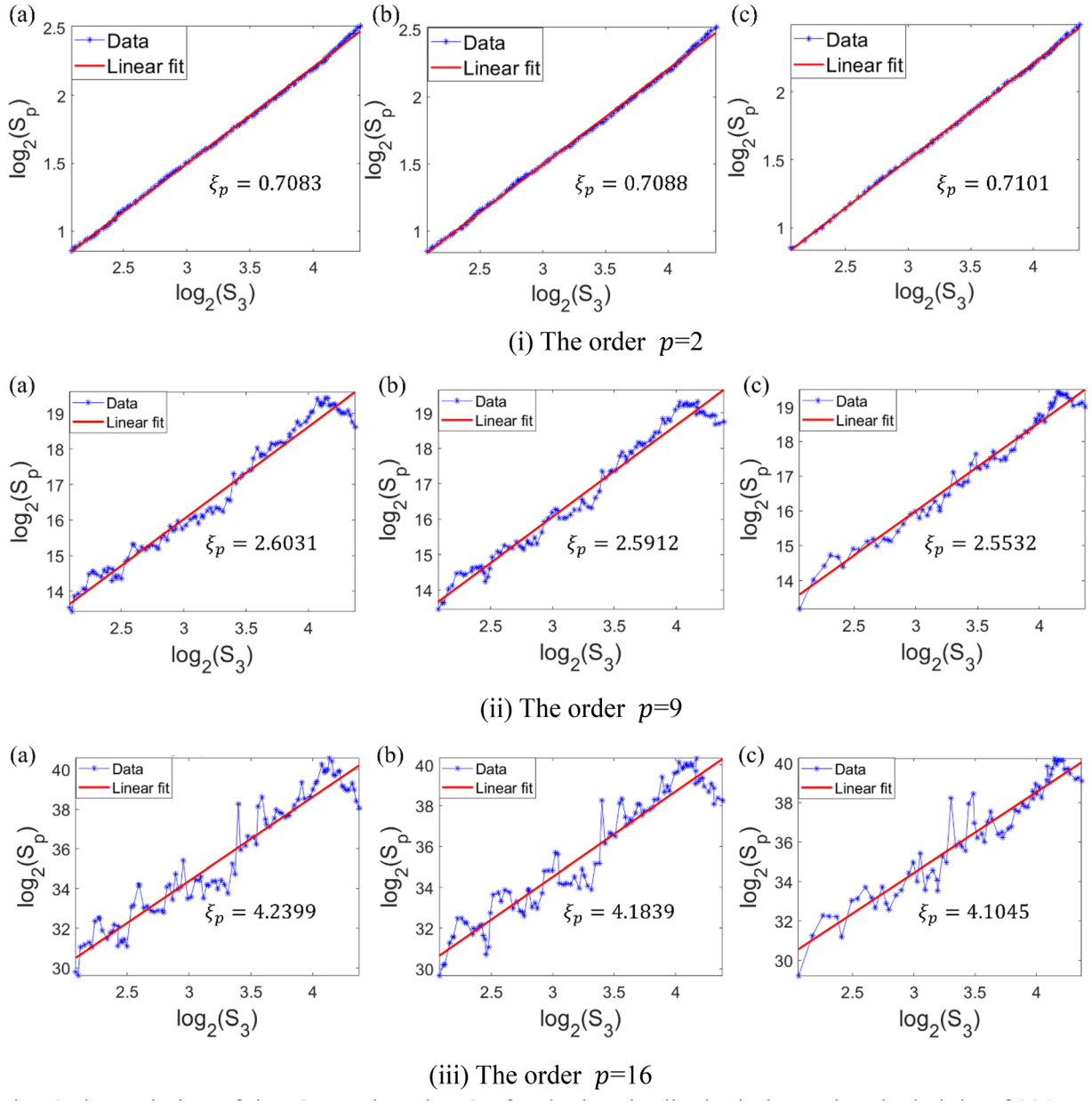

FIG. 6. The variation of S_p against S_3 for the longitudinal wind speed at a height of 320 m utilizing (a) WT-based TVM, (b) EMD-based TVM, and (c) constant mean.

present the empirical relations of ξ_p with p including the aforementioned K41, K62, SL, and β models. The analysis results demonstrate that the SL model presents a better description for the longitudinal wind speed sample at the height of 160 m, while the advanced β model is more appropriate to describe the relationship between ξ_p and p at the other two heights. In terms of the lateral scaling exponent, there exists a gradual decrease with increase in the measured height, especially for the high order p from Fig. 8. It should be noted that while the K41 model presents the best description for the lateral wind speed sample measured at the height of 40 m, four models are not enough to accurately describe the relationship between ξ_p and p at the other two heights.

The absolute error (AE) and relative error (RE) were adopted to quantify the discrepancies of scaling exponents ξ_p, given by

$$AE = \xi_{pI} - \xi_{pO} \quad RE = \frac{\xi_{pI} - \xi_{pO}}{\xi_{pO}}, \tag{17}$$

where ξ_{pI} and ξ_{pO} were respectively determined by the new (i.e., using the WT-based TVM and EMD-based TVM) and original approaches

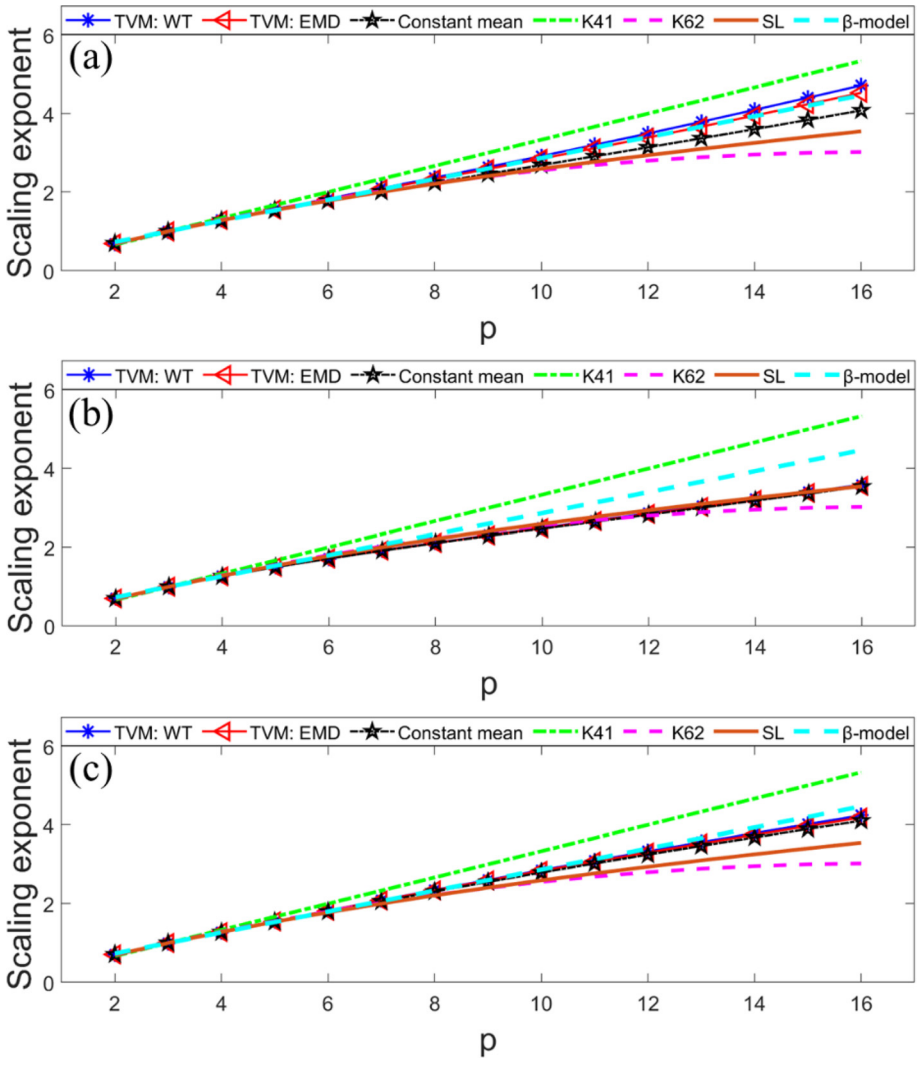

FIG. 7. The change in scaling exponent ξ_p of longitudinal wind speed samples with the order p at heights of (a) 40 m, (b) 160 m, and (c) 320 m.

(utilizing the constant mean). Errors of scaling exponents ξ_p depicted in Figs. 7 and 8 are provided in Figs. 9 and 10, showing that the defined errors of the parameters ξ_p are almost the same for the order p less than 5 obtained by different approaches. However, it dramatically rises with the order p for p values greater than 5. Given that the absolute values of the *RE* and *AE* obtained from the WT-based method are generally larger than those derived from the EMD-based approach, as shown in Figs. 9 and 10, it can be inferred that the more detailed extraction of the TVM for longitudinal nonstationary wind speeds results in greater defined errors in the scaling exponents.

The 95% confidence intervals for the scaling exponents of 526 consecutive 10-min longitudinal wind speed samples during Typhoon Mangkhut obtained by different methods are reported at the orders $p = 2$–9 in Table I. For comparison, Table I also presents some previous experiment results, where "Arneodo, ESS" denotes the result from various open turbulent flows in Arneodo *et al.* (1996) utilizing the ESS method; the term "Saw, ESS" was given by Saw *et al.* (2018) using the ESS method for the velocity field in a von Karman setup without the use of the Taylor hypothesis, where the measurements are made using the PIV method at four different ranges of spatial scales. In addition, "Saw, global" results are also obtained from Saw *et al.* (2018), in which the nondimensionalized structure functions were conjoined (using mean energy dissipation rate $\langle\varepsilon\rangle$ and the dissipation scale η) and the curve fitting was then conducted to the combined structure functions to obtain the global estimates of scaling exponents. The results from the three methods show notable differences in scaling exponents across orders p from 2 to 9, especially when compared to previous results such as "Arneodo, ESS," "Saw, ESS," and "Saw, global." The WT-based TVM method yielded consistent values, with $p = 2$ exponents around 0.7155–0.7234, reaching approximately 2.0618 at $p = 9$. In contrast, "Arneodo, ESS" and "Saw, ESS" generally report higher scaling exponents, suggesting that WT-based TVM may provide a more conservative estimate. The EMD-based TVM results were similar but slightly lower, peaking at about 2.0599 for $p = 9$. The constant mean method generally produced the lowest values. Compared to "Saw, global," which uses combined structure functions for estimates, these findings

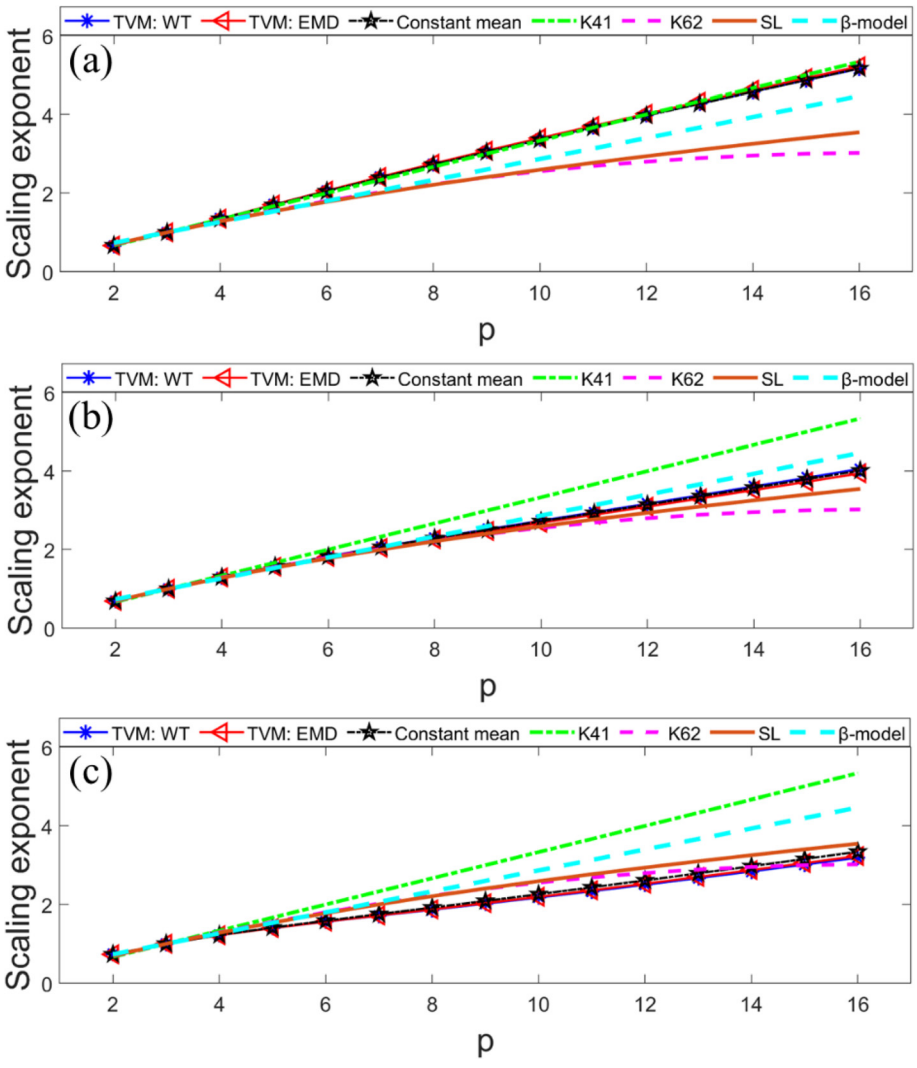

FIG. 8. The change in scaling exponent ξ_p of lateral wind speed samples with the order p at heights of (a) 40 m, (b) 160 m, and (c) 320 m.

highlight the sensitivity of results to methodological choices, emphasizing the need for careful consideration in future studies on turbulent flows during extreme weather events like Typhoon Mangkhut.

IV. SCALING PROPERTIES OF NONSTATIONARY DOWNBURST WIND FIELDS

A. Data source

The 2002 Thunderstorm Outflow Experiment, conducted by the Department of Atmospheric Science at Texas Tech University from May 20 to July 15, 2002, aimed to acquire high-resolution data regarding the kinematic and thermodynamic surface structure of thunderstorm outflows. For this purpose, seven portable towers were arranged in a linear north–south orientation at the Reese Technology Center in Lubbock, Texas, where the landscape is exceptionally flat. On June 4 of that year, the propagation of a rear-flank downdraft (RFD) outflow occurred perpendicularly through the tower array. The wind speed time series obtained concurrently from the varying elevations of 2, 4, 6, 10, and 15 meters with a sampling rate of 1.0 Hz at Tower 4 are depicted in Fig. 11. A detailed description can be found in Chen and Letchford (2005, 2006).

B. The comparison of scaling exponents

The TVMs of wind speed histories, extracted by WT-based and EMD-based methods, are shown in Fig. 12(a), which demonstrates that the TVM obtained from the WT-based method captures more detailed local variation in wind speeds compared to both the EMD-based TVM and the constant mean wind speed. The nonstationary wind speed at a height of 15 m was employed at a reference to present the detailed analysis process of scaling exponents, as shown in Fig. 12(b). It should be noted that the downburst wind speed sample shown in Fig. 12 exhibits stronger nonstationarity than the Typhoon Mangkhut case given in Fig. 3.

Similar to Sec. III B, the natural logarithm of the probability density function F of the wind velocity increments for the nonstationary downburst RFD at the height of 15 m was computed based on different

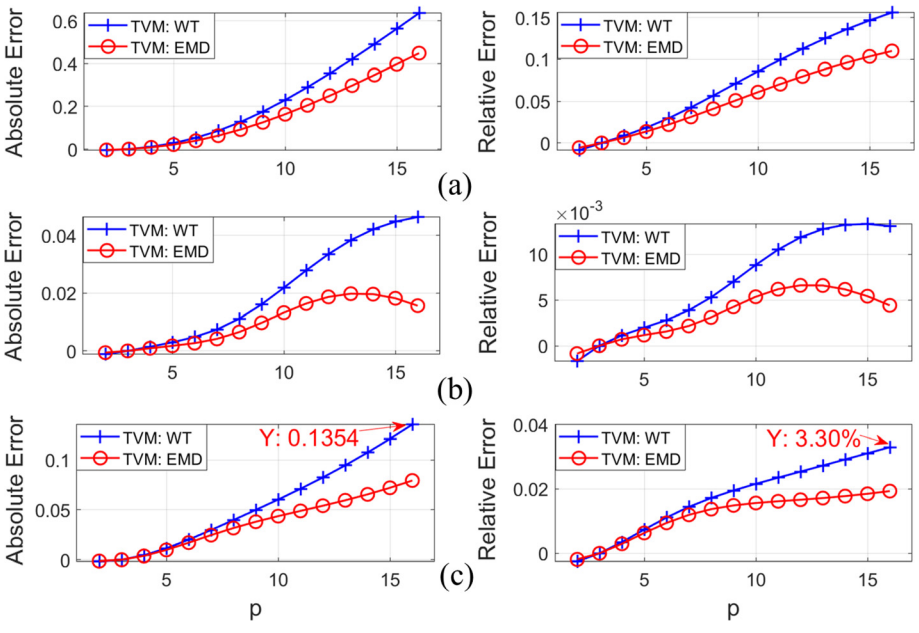

FIG. 9. Associated errors for the longitudinal scaling exponent at heights of (a) 40 m, (b) 160 m, and (c) 320 m.

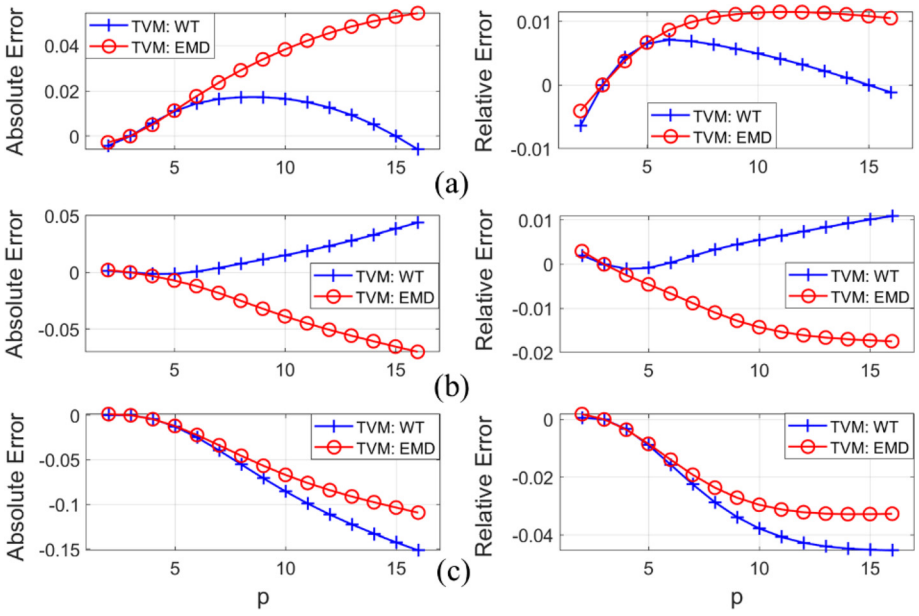

FIG. 10. Associated errors for the lateral scaling exponent at heights of (a) 40 m, (b) 160 m, and (c) 320 m.

methods at a spatial distance of L1 = 20 m, L2 = 50 m, and L3 = 150 m, as shown in Fig. 13, which indicates that the probability distribution for the same spatial distances based on different approaches was only similar in the middle part. In addition, Fig. 13 reveals that the larger the separation distances, the flatter the probability distribution maps become. The skewness and kurtosis of velocity increments with the increase in separation distances utilizing different approaches were obtained and are presented in Fig. 14. Compared to the analysis results for the Typhoon event revealed in Fig. 5, the kurtosis of the velocity increments of nonstationary downburst wind fields shows a similar decreasing trend with increasing separation distance, which verifies the observation from Fig. 13 that with increasing separation distances, the probability distribution maps grow increasingly flat. Differently from the Typhoon event, the disparities in both kurtosis and skewness for the nonstationary downburst are pronounced when using the WT-based TVM, EMD-based TVM, and constant mean. This is likely due to the stronger nonstationarity in the time history of the downburst, as revealed in Figs. 3 and 12.

The variation of S_p against S_3 for the nonstationary downburst RFD at orders $p = 2$, 9, and 16 is provided in Fig. 15. The strong linear

TABLE I. Comparison of scaling exponents between this paper for 526 consecutive 10-min longitudinal wind speed samples during Typhoon Mangkhut and previous experiment results.

Order		p = 2	p = 3	p = 4	p = 5	p = 6	p = 7	p = 8	p = 9	Configuration
"Arneodo, ESS"		[0.67, 0.73]	1	[1.25, 1.31]	[1.50, 1.60]	[1.72, 1.82]	[1.98, 2.08]	[2.12, 2.28]	[2.33, 2.43]	Swirling flow, wind tunnel, downstream of grid and jet
"Saw, ESS"		[0.685, 0.695]	1	[1.285, 1.295]	[1.54, 1.56]	[1.78, 1.82]	[1.99, 2.05]	[2.19, 2.26]	[2.36, 2.46]	von Kármán flows
"Saw, global"		[0.65, 0.71]	1	[1.26, 1.33]	[1.54, 1.61]	[1.79, 1.86]	[2.02, 2.08]	[2.30, 2.39]	[2.52, 2.61]	von Kármán flows
40 m	using WT-based TVM	[0.7215, 0.7249]	1	[1.2227, 1.2290]	[1.4034, 1.4177]	[1.5542, 1.5767]	[1.6852, 1.7162]	[1.8094, 1.8500]	[1.9277, 1.9768]	Typhoon Mangkhut
	using EMD-based TVM	[0.7210, 0.7245]	1	[1.2219, 1.2282]	[1.3987, 1.4130]	[1.5442, 1.5670]	[1.6775, 1.7100]	[1.8019, 1.8432]	[1.9249, 1.9744]	
	using constant mean	[0.7208, 0.7242]	1	[1.2209, 1.2270]	[1.3996, 1.4137]	[1.5526, 1.5754]	[1.6907, 1.7219]	[1.8158, 1.8565]	[1.9248, 1.9748]	
160 m	using WT-based TVM	[0.7155, 0.7192]	1	[1.2293, 1.2366]	[1.4143, 1.4310]	[1.5750, 1.6009]	[1.7260, 1.7608]	[1.8714, 1.9146]	[2.0103, 2.0618]	
	using EMD-based TVM	[0.7160, 0.7198]	1	[1.2293, 1.2365]	[1.4153, 1.4318]	[1.5666, 1.5929]	[1.7151, 1.7504]	[1.8593, 1.9028]	[2.0093, 2.0599]	
	using constant mean	[0.7157, 0.7196]	1	[1.2269, 1.2345]	[1.4102, 1.4272]	[1.5715, 1.5980]	[1.7255, 1.7610]	[1.8710, 1.9152]	[2.0212, 2.0725]	
320 m	using WT-based TVM	[0.7234, 0.7289]	1	[1.2138, 1.2233]	[1.3881, 1.4080]	[1.5476, 1.5783]	[1.6935, 1.7351]	[1.8173, 1.8694]	[1.9526, 2.0139]	
	using EMD-based TVM	[0.7243, 0.7298]	1	[1.2143, 1.2237]	[1.3904, 1.4100]	[1.5455, 1.5756]	[1.6860, 1.7262]	[1.8197, 1.8707]	[1.9485, 2.0098]	
	using constant mean	[0.7248, 0.7304]	1	[1.2127, 1.2222]	[1.3868, 1.4062]	[1.5404, 1.5703]	[1.6789, 1.7193]	[1.8179, 1.8679]	[1.9462, 2.0061]	

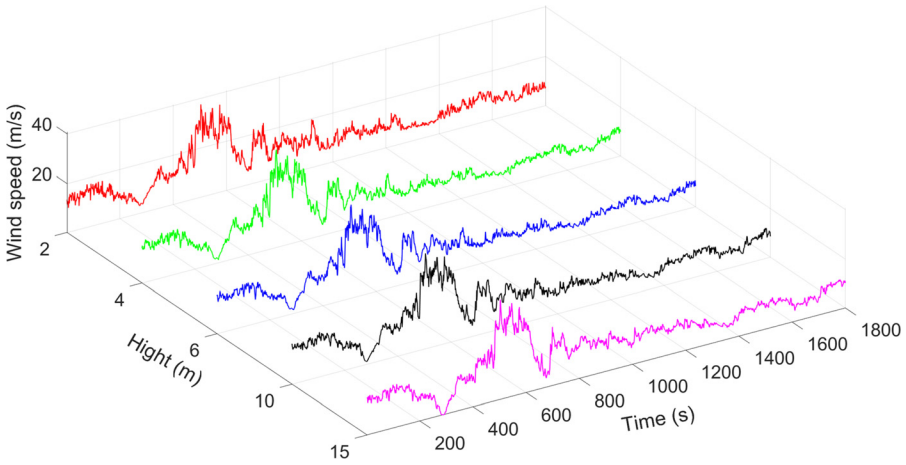

FIG. 11. Wind speed time histories of RFD.

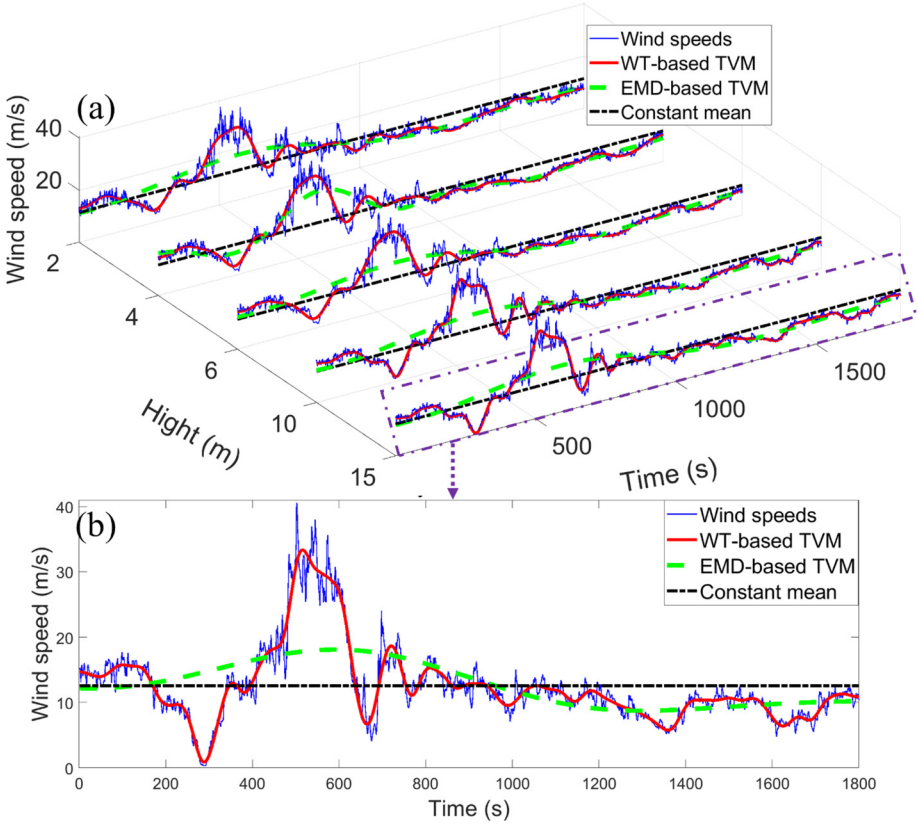

FIG. 12. The wind speed histories and TVMs of the nonstationary downburst RFD.

relation between $\log_2(S_p(r))$ and $\log_2(S_3(r))$ in Fig. 15 for the low order $p = 2$ verifies the validity of the ESS method for computing the scaling exponent ξ_p of the nonstationary downburst RFD. It is observed in Fig. 15 that as the order p increases, the linear relationship of $\log_2(S_p(r))$ and $\log_2(S_3(r))$ gradually weakens. In spite of this observation, a convincing scaling exponent of the nonstationary downburst RFD at the higher order p can still be obtained by using the ESS method from Fig. 15.

The scaling exponents of nonstationary downburst RFD measured at five heights are described in Fig. 16. The analysis results demonstrate that the SL model presents a better description for the nonstationary downburst RFD at heights 2 and 6 m, while the K62 model is more appropriate to describe the relationship between ξ_p and p at the height of 10 m. For the wind speed sample at the remaining two heights, the efficacy of SL model and K62 model in expressing the observed phenomena is comparable.

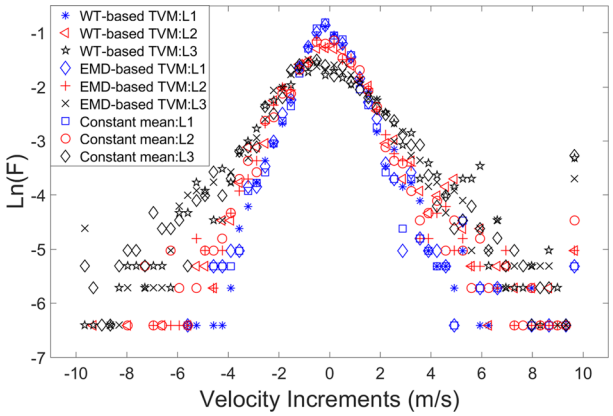

FIG. 13. The natural logarithm of the probability density function F of the wind velocity increments at the height of 15 m.

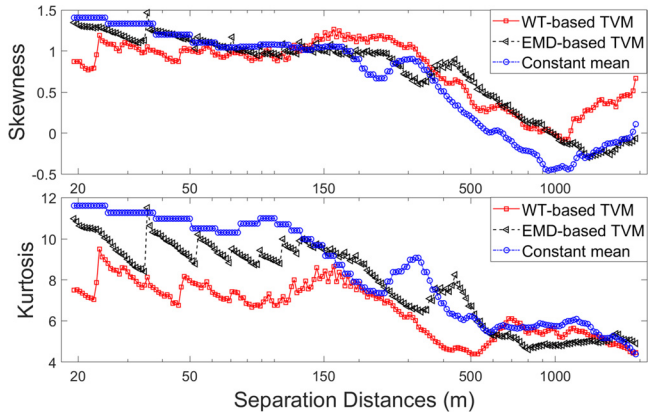

FIG. 14. The skewness and kurtosis of velocity increments at the height of 15 m with increase in separation distances utilizing different approaches.

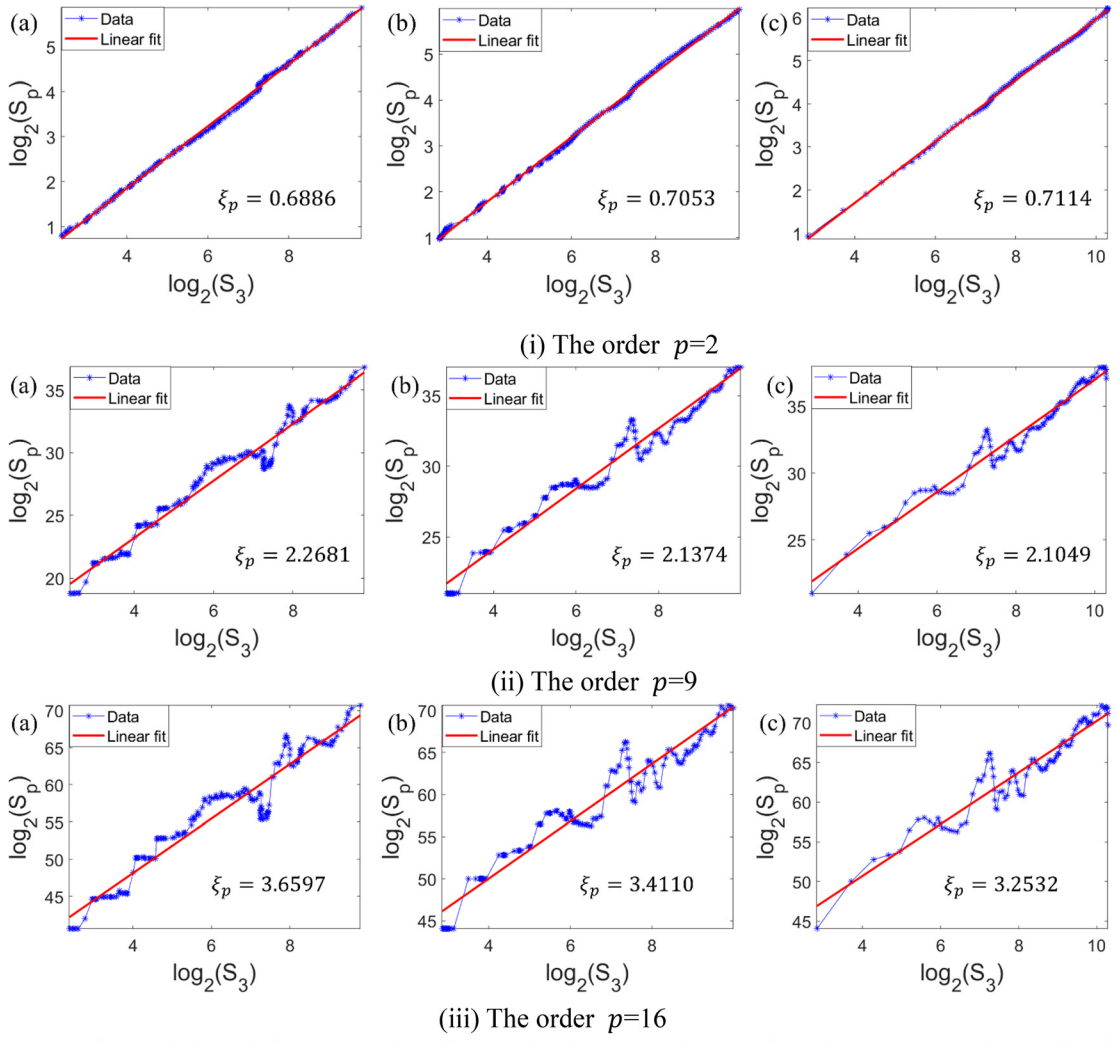

FIG. 15. The variation of S_p against S_3 for the nonstationary downburst RFD at the height of 15 m utilizing (a) WT-based TVM, (b) EMD-based TVM, and (c) constant mean.

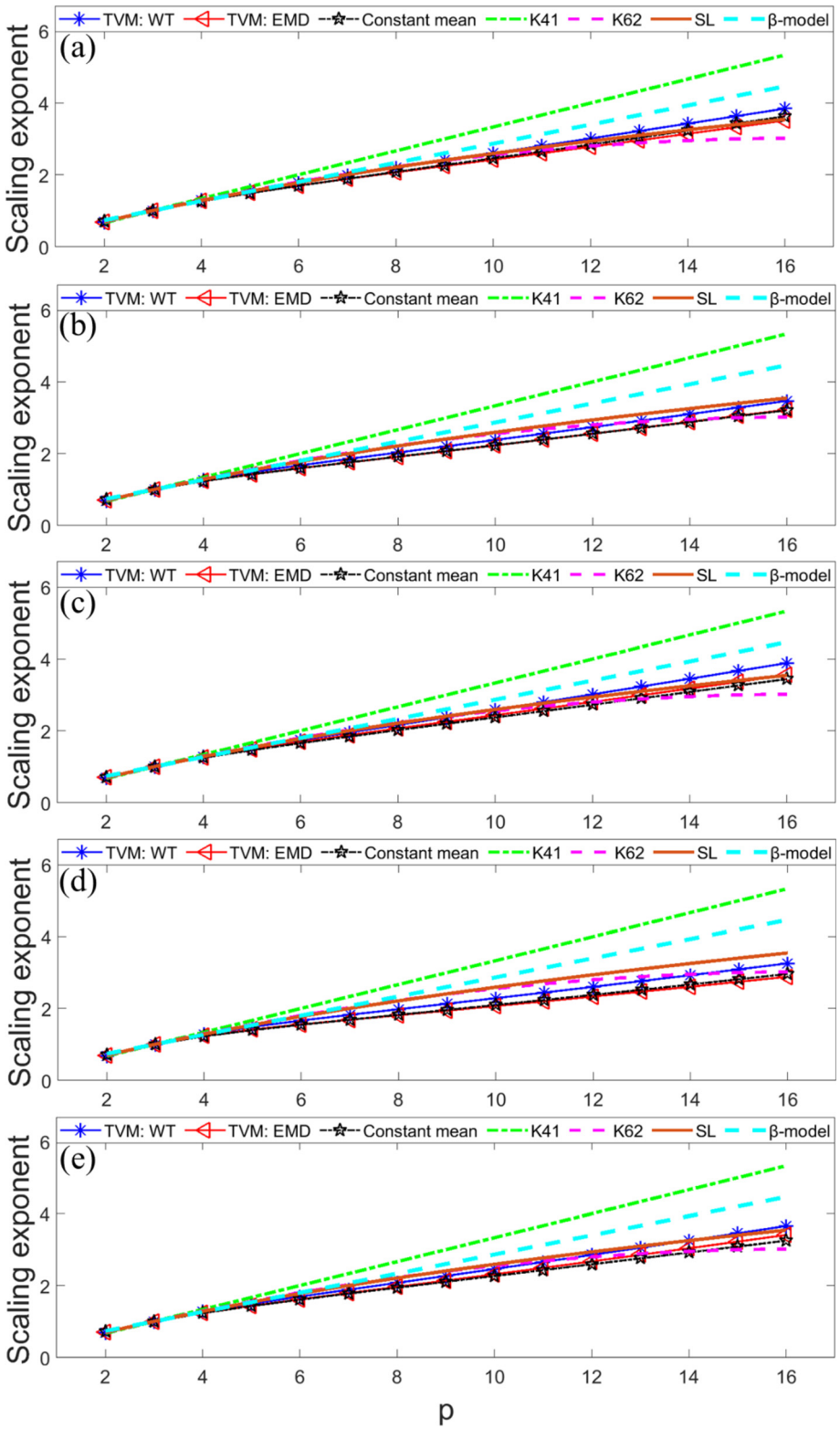

FIG. 16. The change of the scaling exponent ξ_p of nonstationary downburst RFD with the order p at heights of (a) 2 m, (b) 4 m, (c) 6 m, (d) 10 m, and (e) 15 m.

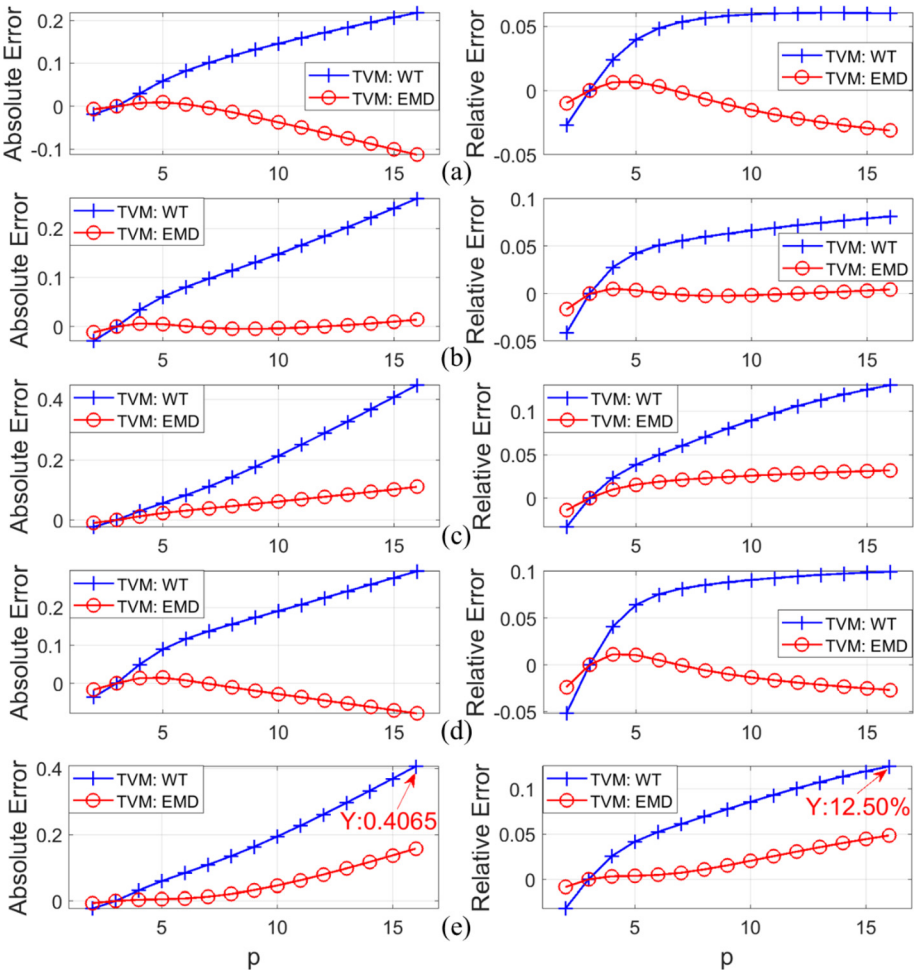

FIG. 17. Associated errors for the scaling exponent of the nonstationary downburst RFD at heights of (a) 2 m, (b) 4 m, (c) 6 m, (d) 10 m, and (e) 15 m.

The associated errors given in Fig. 17 show that the values of the *AE* and *RE* dramatically rise with the order p when using the WT-based method. In comparison, the variations in *AE* and *RE* with p are much smaller when utilizing the EMD-based approach. Furthermore, the absolute values of the RE and AE obtained using the WT-based method are generally larger than those derived using the EMD-based method, as shown in Fig. 17. It can be inferred that the more detailed extraction of the TVM of the nonstationary downburst RFD leads to greater defined errors in the scaling exponents. In addition, as noted in Fig. 9(c) and Fig. 17(e), the maximum values of *AE* and *RE* for the wind speed sample of nonstationary downburst RFD at a height of 15 m shown in Fig. 12(b) are respectively 0.4065 and 12.50%, occurring at the order $p = 16$ when using the WT-based method, which are significantly greater than the *AE* of 0.1354 and *RE* of 3.30% observed for the wind speed sample of Typhoon Mangkhut at a height of 320 m provided in Fig. 3. This observation leads to the inference that stronger nonstationarity will result in larger defined errors in the scaling exponents. This suggests that the Taylor's frozen hypothesis methods need to be adjusted when computing the scaling exponents ξ_p of nonstationary wind speeds in future studies, particularly for those with strong nonstationarity.

V. CONCLUSIONS

This paper focuses on the improvement of Taylor's frozen hypothesis to study the scaling properties of velocity increment of nonstationary wind fields. According to the original Taylor's frozen hypothesis, it assumes that the mean wind speed $\bar{U}$ remains constant and the spatial distance r is determined by $r = \bar{U} \cdot \Delta t$. Using this relationship, the structure function $S_p(r)$ can be obtained by $S_p(r) = \left\langle \left| u(t_i + \Delta t) - u(t_i) \right|^p \right\rangle$. The key step of the new approach is to substitute the time-varying mean component $\bar{U}(t)$ of nonstationary wind speeds for the constant mean $\bar{U}$. As a result, the spatial distance r_m and structure function $S_p(r_m)$ of nonstationary wind speed fields are modified as $r_m = \int_{t_i}^{t_i+\Delta t_{i,m}} \bar{U}(t)dt$ and $S_p(r_m) = \left\langle \left| u(t_i + \Delta t_{i,m}) - u(t_i) \right|^p \right\rangle$, respectively. It should be noted that the time gap $\Delta t_{i,m}$ is not fixed for a given r_m, but varies with the position x or time t, as $\bar{U}(t)$ is time-variant. Detailed comparisons of the scaling properties of wind speed data measured during Typhoon Mangkhut and downburst RFD were conducted employing different methodologies. The main conclusions of this study are as follows:

(a) Analysis results reveal that the kurtosis of the velocity increments shows a decreasing trend with increasing separation distance utilizing different approaches.
(b) The strong linear relation between $\log_2(S_p(r))$ and $\log_2(S_3(r))$ for the low order p verifies the validity of the ESS method for computing the scaling exponent ξ_p of nonstationary wind fields. As the order p increases, the linear relationship of $\log_2(S_p(r))$ and $\log_2(S_3(r))$ gradually weakens. In spite of this observation, a convincing scaling exponent of the nonstationary wind speeds at the higher order p can still be obtained by using the ESS method.
(c) The results clearly demonstrate that the various models, including the K41 model, K62 model, SL model, and β model, have their own strengths and limitations. Significant differences in scaling exponents are observed between the original and new versions of Taylor's hypothesis, particularly at the higher order of p or for the case of wind speed with strong nonstationarity such as the downburst event. It is thus more reasonable that the new approach should be employed to conduct a more precise scaling analysis of nonstationary wind fields.

ACKNOWLEDGMENTS

The work described in this paper was partially supported by the National Natural Science Foundation of China (Grant Nos. 52478564 and 52178512), Ningbo Key R&D Program (Project Nos. 2023Z221 and 2024Z287), and Research Grants Council of Hong Kong Theme-based Research Scheme (Grant No. T22-501/23-R).

AUTHOR DECLARATIONS

Conflict of Interest

The authors have no conflicts to disclose.

Author Contributions

Kang Cai: Conceptualization (equal); Data curation (equal); Formal analysis (equal); Investigation (equal); Methodology (equal); Resources (equal); Software (equal); Validation (equal); Visualization (equal); Writing – original draft (equal); Writing – review & editing (equal). **Ming feng Huang:** Conceptualization (equal); Funding acquisition (equal); Project administration (equal); Resources (equal); Supervision (equal); Writing – review & editing (equal). **Jiayao Wang:** Supervision (equal); Validation (equal); Visualization (equal); Writing – review & editing (equal). **You Dong:** Writing – review & editing (equal). **Yi-Qing Ni:** Funding acquisition (equal); Writing – review & editing (equal). **Pak Wai Chan:** Writing – review & editing (equal).

DATA AVAILABILITY

Some or all data, models, or codes that support the findings of this study are available from the corresponding author upon reasonable request.

REFERENCES

Ali, N., Aseyev, A. S., and Cal, R. B., "Structure functions, scaling exponents and intermittency in the wake of a wind turbine array," J. Renewable Sustainable Energy **8**(1), 013304 (2016).
Arneodo, A., Baudet, C., Belin, F., Benzi, R., Castaing, B *et al.*, "Structure functions in turbulence, in various flow configurations, at Reynolds number between 30 and 5000, using extended self-similarity," Europhys. Lett. **34**(6), 411–416 (1996).
Babiano, A., Dubrulle, B., and Frick, P., "Some properties of two-dimensional inverse energy cascade dynamics," Phys. Rev. E **55**(3), 2693–2706 (1997).
Benzi, R., Ciliberto, S., Tripiccione, R., Baudet, C., Massaioli, F., and Succi, S., "Extended self-similarity in turbulent flows," Phys. Rev. E **48**(1), R29–R32 (1993).
Böttcher, F., Barth, S., and Peinke, J., "Small and large scale fluctuations in atmospheric wind speeds," Stoch. Environ. Res. Ris. Assess. **21**, 299–308 (2007).
Briscolini, M., Santangelo, P., Succi, S., and Benzi, R., "Extended self-similarity in the numerical simulation of three-dimensional homogeneous flows," Phys. Rev. E **50**(3), R1745–R1747 (1994).
Cai, K., Huang, M. F., Xu, H. W., and Kareem, A., "Analysis of nonstationary typhoon winds based on optimal time-varying mean wind speed," J. Struct. Eng. **148**(12), 04022199 (2022).
Cai, K., Li, X., and Zhi, L. H., "Extracting time-varying mean component of non-stationary winds utilizing vondrak filter and genetic algorithm: A wind engineering perspective," Int. J. Struct. Stab. Dyn. **21**(11), 2150155 (2021a).
Cai, K., Li, X., Zhi, L. H., and Han, X. L., "Extraction of optimal time-varying mean of non-stationary wind speeds based on empirical mode decomposition," Struct. Eng. Mech. **77**(3), 355–368 (2021b).
Chen, L. and Letchford, C. W., "Proper orthogonal decomposition of two vertical profiles of full-scale nonstationary downburst wind speeds," J. Wind Eng. Ind Aerodyn. **93**(3), 187–216 (2005).
Chen, L. and Letchford, C. W., "Multi-scale correlation analyses of two lateral profiles of full-scale downburst wind speeds," J. Wind Eng. Ind Aerodyn. **94**(9), 675–696 (2006).
Chen, J., Hui, M. C. H., and Xu, Y. L., "A comparative study of stationary and non-stationary wind models using field measurements," Boundary. Layer Meteorol. **122**(1), 105–121 (2007).
Frisch, U. and Kolmogorov, A. N., *Turbulence: The Legacy of an Kolmogorov* (Cambridge University Press, 1995).
Frisch, U., Sulem, P., and Nelkin, M., "A simple dynamical model of intermittent fully developed turbulence," J. Fluid Mech. **87**(4), 719–736 (1978).
Galtier, S., *Introduction to Modern Magnetohydrodynamics* (Cambridge University Press, Cambridge, 2016).
Gaudin, E., Protas, B., Goujon-Durand, S., Wojciechowski, J., and Wesfreid, J. E., "Spatial properties of velocity structure functions in turbulent wake flows," Phys. Rev. E **57**(1), R9–R12 (1998).
Gurley, K. and Kareem, A., "Analysis interpretation modeling and simulation of unsteady wind and pressure data," J. Wind Eng. Ind Aerodyn. **69–71**(1), 657–669 (1997).
Harris, V. G., Graham, J. A. H., and Corrsin, S., "Further experiments in nearly homogeneous turbulent shear flow," J. Fluid Mech. **81**(4), 657–687 (1977).
Jung, S. and Masters, F. J., "Characterization of open and suburban boundary layer wind turbulence in 2008 hurricane Ike," Wind Struct. **17**(2), 135–162 (2013).
Kolmogorov, A. N., "The local structure of turbulence in incompressible viscous fluid for very large Reynolds' numbers," Proc. USSR Acad. Sci. **30**, 301–305 (1941), available at https://scispace.com/papers/the-local-structure-of-turbulence-in-incompressible-viscous-25te3acxv9.
Kolmogorov, A., "A refinement of previous hypotheses concerning the local structure of turbulence in a viscous incompressible fluid at high Reynolds number," J. Fluid Mech. **13**(1), 82–85 (1962).
Meneveau, C. and Sreenivasan, K., "The multifractal nature of turbulent energy dissipation," J. Fluid Mech. **224**, 429–484 (1991).
Ruiz-Chavarria, G., Ciliberto, S., Baudet, C., and Lévêque, E., "Scaling properties of the streamwise component of velocity in a turbulent boundary layer," Phys. D **141**(3–4), 183–198 (2000).
Saw, E. W., Debue, P., Kuzzay, D., Daviaud, F., and Dubrulle, B., "On the universality of anomalous scaling exponents of structure functions in turbulent flows," J. Fluid Mech. **837**, 657–669 (2018).
Saw, E. W., Kuzzay, D., Faranda, D., Guittonneau, A., Daviaud, F., Wiertel-Gasquet, C., Padilla, V., and Dubrulle, B., "Experimental characterization of extreme events of inertial dissipation in a turbulent swirling flow," Nat. Commun. **7**, 12466 (2016).
She, Z. S. and Leveque, E., "Universal scaling laws in fully developed turbulence," Phys. Rev. Lett. **72**(3), 336–339 (1994).
Solari, G., De Gaetano, P., and Repetto, M. P., "Thunderstorm response spectrum: Fundamentals and case study," J. Wind Eng. Ind Aerodyn. **143**, 62–77 (2015).

Taylor, G. I., "The spectrum of turbulence," Proc. R. Soc. Lond. A. **164**, 476–490 (1938).
Vincent, A. and Meneguzzi, M., "The spatial structure and statistical properties of homogeneous turbulence," J. Fluid Mech. **225**, 1–20 (1991).
Vindel, J. M., Yagüe, C., and Redondo, J. M., "Structure function analysis and intermittency in the atmospheric boundary layer," Nonlinear Processes Geophys. **15**, 915–929 (2008).
Water, W. V. and Herweijer, J., "High-order structure functions of turbulence," J. Fluid Mech. **387**, 3–37 (1999).
Wood, G. S., Kwok, K. C. S., Motteram, N. A., and Fletcher, D. F., "Physical and numerical modelling of thunderstorm downbursts," J. Wind Eng. Ind Aerodyn. **89**(6), 535–552 (2001).
Xu, Y. L. and Chen, J., "Characterizing nonstationary wind speed using empirical mode decomposition," J. Struct. Eng. **130**(6), 912–920 (2004).